

NIR-Assisted Image Denoising: A Selective Fusion Approach and A Real-World Benchmark Dataset

Rongjian Xu, Zhilu Zhang, Renlong Wu, and Wangmeng Zuo, *Senior Member, IEEE*

arXiv:2404.08514v2 [cs.CV] 16 Apr 2024

Abstract—Despite the significant progress in image denoising, it is still challenging to restore fine-scale details while removing noise, especially in extremely low-light environments. Leveraging near-infrared (NIR) images to assist visible RGB image denoising shows the potential to address this issue, becoming a promising technology. Nonetheless, existing works still struggle with taking advantage of NIR information effectively for real-world image denoising, due to the content inconsistency between NIR-RGB images and the scarcity of real-world paired datasets. To alleviate the problem, we propose an efficient Selective Fusion Module (SFM), which can be plug-and-played into the advanced denoising networks to merge the deep NIR-RGB features. Specifically, we sequentially perform the global and local modulation for NIR and RGB features, and then integrate the two modulated features. Furthermore, we present a Real-world NIR-Assisted Image Denoising (Real-NAID) dataset, which covers diverse scenarios as well as various noise levels. Extensive experiments on both synthetic and our real-world datasets demonstrate that the proposed method achieves better results than state-of-the-art ones. The dataset, codes, and pre-trained models will be publicly available at <https://github.com/ronjonxu/NAID>.

Index Terms—NIR-assisted image denoising, Real-world, Dataset.

I. INTRODUCTION

IN low-light conditions, it's common to use short exposure time and high ISO in imaging to prevent motion blur, while this setting inevitably introduces noise due to the limited number of photons captured by camera. With the development of deep learning [1]–[3], many image denoising methods [4]–[10] have been proposed to remove the noise. Although great progress has been achieved, it is still challenging for these methods to recover fine-scale details faithfully due to the severely ill-posed nature of denoising. An alternative solution is multi-frame denoising [11]–[16], in which multiple successive frames are merged to improve performance. However, it is susceptible to the misalignment between frames, and may be less effective in facing dynamic scenes.

Fortunately, near-infrared (NIR) images with low noise can be captured at a cheap cost and utilized to enhance the denoising of visible RGB images [17]–[20], dubbed NIR-Assisted Image Denoising (NAID). Specifically, on the one hand, the NIR band lies outside the range of the human visible spectrum. It enables us to turn on NIR light that is

R. Xu is with the Faculty of Computing, Harbin Institute of Technology, Harbin, China. (E-mail: ronjon.xu@gmail.com)

Z. Zhang is with the Faculty of Computing, Harbin Institute of Technology, Harbin, China. (E-mail: cszlzhang@outlook.com)

R. Wu is with the Faculty of Computing, Harbin Institute of Technology, Harbin, China. (E-mail:hirenlongwu@gmail.com)

W. Zuo is with the Faculty of Computing, Harbin Institute of Technology, Harbin, China. (E-mail: wmzuo@hit.edu.cn)

imperceptible to humans, thus capturing NIR images [21] with a low noise level. On the other hand, modern CMOS sensors are sensitive to partial near-infrared wavelengths [22], thus allowing NIR signals to be acquired cheaply and conveniently.

Nevertheless, the inconsistencies between NIR and RGB contents limit the positive effect of NIR images in denoising. Firstly, NIR images are captured under additional NIR light and are monochromatic, which leads to brightness and color discrepancies between the two modalities. Secondly, the NIR images may ‘more-see’ or ‘less-see’ the objects than the visible light ones, primarily due to inherent differences in the optical properties within each spectral domain [21]. For example, as shown in Fig. 1 (a), the RGB image clearly contains textual information, while the corresponding NIR image lacks that. In Fig. 1 (b), the NIR image exhibits extra fruit patterns, while these patterns are absent in the RGB image. DVD [19] and SANet [23] have noticed this problem, but their solutions are complex and less effective.

In this work, we focus on the inconsistency issue and aim to circumvent its adverse effects on combinations of NIR and RGB images in an efficient manner. On the one hand, we introduce a Global Modulation Module (GMM) and a Local Modulation Module (LMM) to deal with color and structure inconsistency issues respectively. They predict and assign soft weights to NIR and RGB features, thus preparing for subsequent feature fusion. The combination of GMM, LMM, and fusion operation is called the Selective Fusion Module (SFM). On the other hand, to take full advantage of advanced denoising network architectures [7], [8], [10], [24], we expect SFM to be integrated into varying networks easily and efficiently. Thus, we design SFM according to the principles of simplicity and pluggability.

Additionally, due to the lack of real-world paired datasets, most existing methods can only process synthetic noisy images. NIR-assisted real-world noise removal is rarely explored. To address the issue, we construct a real-world NAID dataset, named Real-NAID. It encompasses diverse scenarios and various noise levels, providing a valuable resource for evaluating and promoting research in this field. Extensive experiments are conducted on both synthetic DVD [19] and our Real-NAID datasets. The results show that the proposed method performs better than state-of-the-art ones.

Our contributions can be summarized as follows:

(1) For NIR-assisted image denoising, we propose a plug-and-play selective fusion module to handle content inconsistency issues between NIR-RGB images, which assigns appropriate fusion weights to the deep NIR and RGB features by global and local modulation modules.

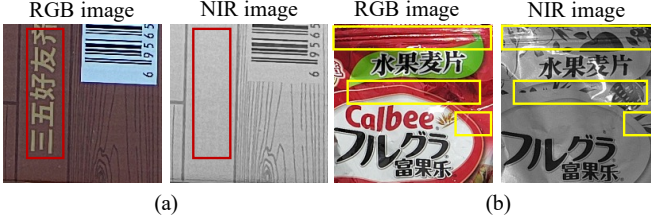


Fig. 1. Examples of the structure discrepancy between NIR-RGB images. (a) The structure is visible in the RGB image but not in the NIR image, as shown in the red box. (b) The structure is visible in the NIR image but not in the RGB image, as shown in the yellow box.

(2) We bring NIR-assisted image denoising to the real world by constructing a paired real-world dataset, which covers diverse scenarios and various noise levels.

(3) Extensive experiments on both synthetic and our real-world datasets demonstrate that the proposed method achieves better than state-of-the-art ones quantitatively and qualitatively.

II. RELATE WORK

A. Single Image Denoising

With the advancements in deep learning [1], [3], [25], numerous single-image denoising methods [4]–[9], [15], [26] have emerged. DnCNN [4] pioneers the utilization of deep learning techniques and surpasses traditional patch-based methods [27]–[29] on Gaussian noise removal. Recently, some methods [7], [8], [24], [30] are developed with advanced architectures. For example, MPRNet [30] applies a multi-stage architecture for progressive image restoration and achieves remarkable performance. Uformer [8] introduces the locally-enhanced transformer by employing the non-overlapping window-based self-attention. Restormer [7] further reduces the computation cost by modifying the self-attention calculation from the spatial dimension to channel one. NAFNet [24] proposes a simple baseline that does not apply nonlinear activation. Despite the significant progress achieved by these methods, the performance is still unsatisfactory when handling images with high-level noise captured under low-light conditions, due to the severely ill-posed nature of denoising.

B. NIR-assisted Image Restoration

Compared to single-image restoration, NIR images have the potential to assist in restoring details from degraded images. The earlier work [31] utilizes gradient constraints for NIR-assisted image denoising. Wang *et al.* [32] further improves the performance with deep learning methods. SSN [18] proposes a multi-task deep network with state synchronization modules. TC-GAN [33] fuses NIR images and RGB ones based on a texture conditional generative adversarial network. DCMAN [34] employs spatial-temporal-spectral priors to introduce NIR videos for low-light RGB video restoration. However, these methods have overlooked the color and structure inconsistency issues between the NIR images and RGB ones. CCDFuse [35] addresses this issue by combining the local modeling ability of convolutional blocks and the non-local modeling ability of

transformer ones to extract local and global features of NIR and RGB images respectively. SANet [23] proposes a guided denoising framework by estimating a clean structure map for the noisy RGB image. Wan *et al.* [20] disentangle the color and structure components from the NIR images and RGB ones. Besides, a few works [19], [36], [37] incorporate different priors into the network design, like sparse coding [36], deep implicit prior [37] and deep inconsistency prior [19]. However, their intricate designs make it difficult to integrate them into existing advanced restoration networks, hindering their extensions and improvements.

C. Datasets for NIR-Assisted Image Restoration

Existing NIR-RGB datasets suffer from limitations such as scarcity of data samples [31], absence of paired real-world RGB noisy images [17], [19], [38], [39], or lack of public accessibility [17], [40]. For instance, Krishnan *et al.* [31] develop a prototype camera to capture image pairs under varying low-light conditions but only containing 5 image pairs. Its size is too small to fulfill the demands of data-driven deep-learning algorithms. IVRG [38] and RGB-NIR Stereo [39] construct datasets consisting of RGB and NIR image pairs for image recognition and stereo matching, respectively. DVD [19] captures images within a controlled light-box environment. However, these datasets only comprise clean RGB and NIR image pairs, lacking real-world noisy RGB images. Burst Dataset [40] captures real-world noisy images by a mobile imaging device that is sensitive to both near-infrared and near-ultraviolet signals. Lv *et al.* [17] introduces the VIS-NIR-MIX dataset which utilizes a motorized rotator to manipulate illumination conditions. But they are not publicly available. In this work, we introduce a real-world NAID benchmark dataset, which encompasses diverse scenarios and various noise levels.

III. REAL-NAID: REAL-WORLD NIR-ASSISTED IMAGE DENOISING DATASET

Existing publicly available NAID datasets generally lack real-world noisy RGB images paired with clean RGB and NIR images, which limits the investigation in real-world NAID. To break such a limitation, we build a real-world NAID dataset, named Real-NAID. Specifically, we employ high ISO and short exposure time to capture the real-world noisy RGB images, as shown in Fig. 2 (a). For capturing the corresponding clean RGB images, we lower the ISO of the camera and appropriately increase the exposure time, as shown in Fig. 2 (b). To obtain paired NIR images, we activate NIR light to ensure a sufficient supply of NIR illumination and then capture them with a dedicated NIR camera, as shown in Fig. 2 (c).

All images are captured with the Huawei X2381-VG surveillance camera, which is equipped with a built-in NIR illuminator specifically designed for capturing NIR images. To ensure image registration among multiple captures, we carefully position the camera and develop a remote control application to capture images of static objects. When capturing clean RGB images, the camera's ISO is set to 600. When capturing RGB images with low, middle, and high noise levels, we set ISO to 4000, 12000, and 32000, respectively. It is worth

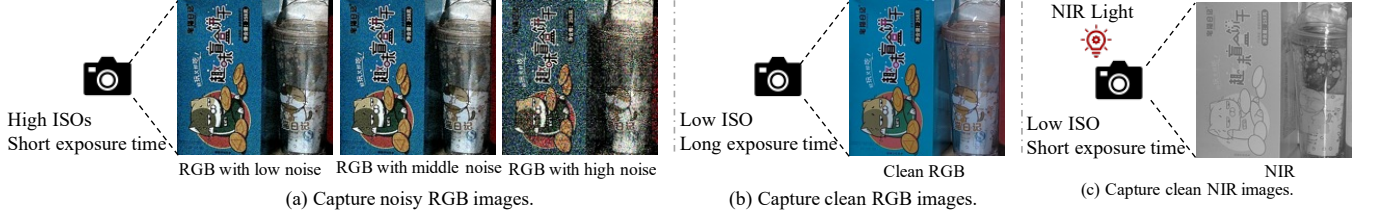


Fig. 2. The construction of Real-NAID dataset. (a) Capture noisy RGB images with three types of high ISO and short exposure time. (b) Capture clean RGB images with low ISO and long exposure time. (c) Turn on the NIR light, then capture the clean NIR images with low ISO and short exposure time.

TABLE I
COMPARISONS OF SOME EXISTING DATASETS CONSISTING OF PAIRED NIR AND RGB IMAGES. ‘PUBLIC’ REFERS TO ITS PUBLIC ACCESSIBILITY. ‘NUMBER’ DENOTES THE NUMBER OF PAIRED IMAGES.

| Dataset | Real-Noise | Public | Number | Resolution |
|-----------------------------|------------|--------|--------|-------------------------|
| RGB-NIR Video [34] | | | 11444 | 1280×720 |
| RGB-NIR Stereo [40] | ✓ | | 42000 | $\sim 582 \times 492$ |
| IVRG [38] | ✓ | | 477 | $\sim 1024 \times 680$ |
| DVD [19] | ✓ | | 307 | 1792×1008 |
| Burst Dataset [40] | ✓ | | 121 | 512×512 |
| VIS-NIR-MIX [17] | ✓ | | 206 | $\sim 3072 \times 2048$ |
| Dark Flash Photography [39] | ✓ | ✓ | 5 | $\sim 1400 \times 1000$ |
| Real-NAID (Ours) | ✓ | ✓ | 300 | 2160×2048 |

noting that we adjust the exposure time of each noise level to keep the brightness of noisy images relatively constant.

Besides, following DVD [19], we crop all images from 2048×3840 resolutions into 2048×2160 to mitigate the vignetting effect. In total, the dataset comprises 100 scenes with diverse contents, and each scene has three noisy images with various noise levels. 70 scenes are randomly sampled as the training set and the remaining 30 ones are used for the testing set. In addition, we compare our Real-NAID dataset with other existing NIR-RGB datasets to demonstrate its strengths, as shown in Table I.

IV. METHOD

A. Problem Formation

NIR-Assisted Image Denoising (NAID) aims at restoring the clean RGB image $\hat{\mathbf{I}} \in \mathbb{R}^{H \times W \times 3}$ from its noisy RGB observation $\mathbf{I}_R \in \mathbb{R}^{H \times W \times 3}$ with the assistance of the NIR image $\mathbf{I}_N \in \mathbb{R}^{H \times W \times 1}$, where H and W denote the height and the width of images, respectively. Compared to the vanilla image denoising based on the multi-scale encoder-decoder architectures as shown in Fig. 3 (a), it further utilizes the corresponding NIR image to guide the noise removal. And this is also the core of the NAID. Assuming that the clean NIR images are perfectly consistent with the noisy RGB ones in color and structure, we can simply adapt the existing denoising architectures in Fig. 3 (a) to Fig. 3 (b). The output $\hat{\mathbf{I}}$ can be written as,

$$\hat{\mathbf{I}} = \mathcal{D}(\mathcal{E}_N(\mathbf{I}_N) + \mathcal{E}_R(\mathbf{I}_R)), \quad (1)$$

where \mathcal{D} denotes the decoder of the denoising network, \mathcal{E}_N and \mathcal{E}_R denote the feature encoders for NIR and RGB images, respectively. However, in practical scenarios, there exist color and structure inconsistencies between the NIR and the RGB

images, as illustrated in Fig. 1. Leveraging the NIR images in a naive way like Eqn. (1) only gains limited performance improvement.

In this work, we suggest alleviating the adverse effects of the inconsistency issue before the combinations of NIR and RGB images. In particular, we propose a Selective Fusion Module (SFM). SFM predicts and assigns soft weights to NIR and RGB features, thus preparing for subsequent feature fusion. Eqn. (1) can be modified to,

$$\hat{\mathbf{I}} = \mathcal{D}(\mathcal{SFM}(\mathcal{E}_N(\mathbf{I}_N), \mathcal{E}_R(\mathbf{I}_R))). \quad (2)$$

Details can be found in the following subsections.

B. Selective Fusion Module

SFM should select valuable information and avoid harmful one from the current NIR-RGB features for feature fusion. To achieve that, we suggest that SFM predicts and assigns pixel-wise weights for NIR-RGB features fusion. Denote the current NIR and RGB features from the corresponding encoders by \mathbf{F}_N and \mathbf{F}_R , SFM can be written as,

$$\mathcal{SFM}(\mathbf{F}_N, \mathbf{F}_R) = \mathbf{W}_N \odot \mathbf{F}_N + \mathbf{W}_R \odot \mathbf{F}_R, \quad (3)$$

where \odot is the pixel-wise multiply operation. \mathbf{W}_N and \mathbf{W}_R denote the weights of NIR and RGB features, respectively. In order to model the color and structure discrepancy respectively, we decouple the weight \mathbf{W} (including \mathbf{W}_N and \mathbf{W}_R) into global and local component, *i.e.*, $\mathbf{W} = \mathbf{W}^g \odot \mathbf{W}^l$, where the former one concentrates on the differences in global information and the latter one focuses on the discrepancy in local information between NIR-RGB features. Based on that, we further present a Global Modulation Module (GMM) to estimate \mathbf{W}^g and a Local Modulation Module (LMM) to estimate \mathbf{W}^l , as shown in Fig. 4.

Global Modulation Module. GMM should handle the global color and brightness difference between the NIR and RGB ones. As shown in Fig. 4 (a), it takes the current NIR features \mathbf{F}_N and the RGB ones \mathbf{F}_R as inputs to estimate the NIR global modulation weights \mathbf{W}_N^g and the RGB ones \mathbf{W}_R^g . Detailly, it first concatenates $\mathbf{F}_N \in \mathbb{R}^{C \times H \times W}$ and $\mathbf{F}_R \in \mathbb{R}^{C \times H \times W}$ as inputs, generating initial weights $\mathbf{W}_{\text{init}}^g \in \mathbb{R}^{2C \times H \times W}$ by a 1×1 convolutional layer, two 1×1 blocks and another 1×1 convolutional layer. It can be written as,

$$\mathbf{W}_{\text{init}}^g = \text{Conv}_{1 \times 1}(\text{Blocks}_{1 \times 1}(\text{Conv}_{1 \times 1}([\mathbf{F}_N, \mathbf{F}_R]))),$$

where $\text{Conv}_{1 \times 1}$ denotes the 1×1 convolutional layer and $\text{Blocks}_{1 \times 1}$ denotes two 1×1 blocks. Each 1×1 block

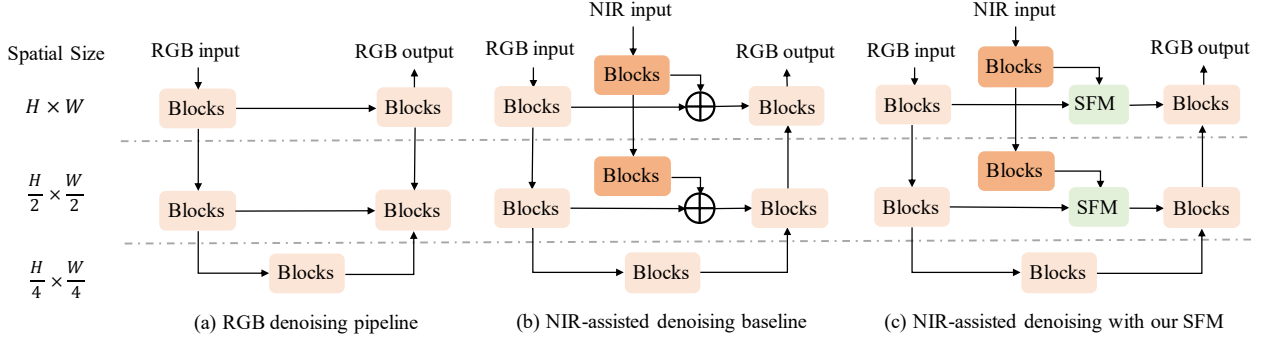


Fig. 3. Comparison of different image denoising manners using multi-scale architecture. (a) RGB image denoising. (b) NIR-assisted RGB image denoising baseline. (c) NIR-assisted RGB image denoising with our proposed SFM.

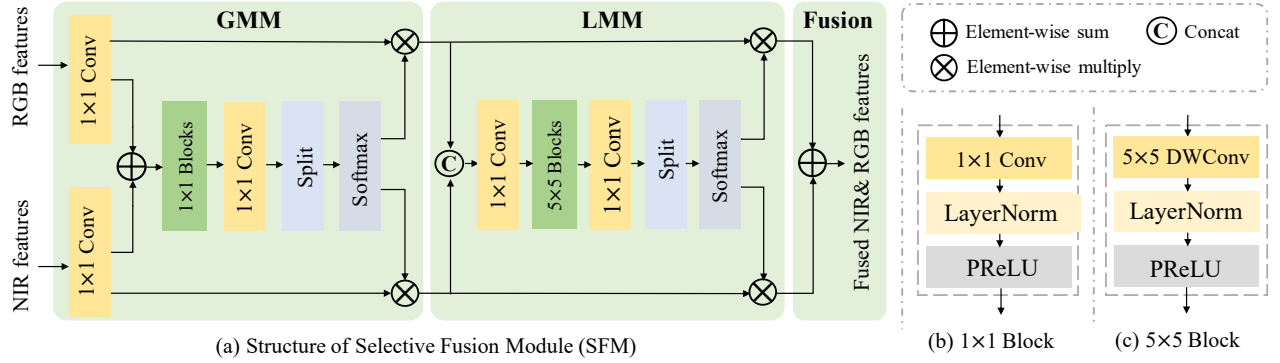


Fig. 4. The structure of our proposed Selective Fusion Module (SFM), where Global Modulation Module (GMM) and Local Modulation Module (LMM) focus on color and structure discrepancy issues between the NIR images and RGB ones, respectively. Two 1×1 blocks and 5×5 blocks are used in GMM and LMM, respectively.

is composed of a 1×1 convolutional layer, a Layer Normalization [41], and a PReLU [42] function, as shown in Fig. 4 (b). Next, $\mathbf{W}_{\text{init}}^g$ is split along channel dimension to get NIR weight maps $\tilde{\mathbf{W}}_{\text{N}}^g \in \mathbb{R}^{C \times H \times W}$ and RGB ones $\tilde{\mathbf{W}}_{\text{R}}^g \in \mathbb{R}^{C \times H \times W}$. Then, a channel-wise softmax operation is applied to $\tilde{\mathbf{W}}_{\text{N}}^g$ and $\tilde{\mathbf{W}}_{\text{R}}^g$, getting the final NIR modulation weights $\mathbf{W}_{\text{N}}^g \in \mathbb{R}^{C \times H \times W}$ and RGB ones $\mathbf{W}_{\text{R}}^g \in \mathbb{R}^{C \times H \times W}$, which can be written as,

$$\begin{aligned} [\mathbf{W}_{\text{N}}^g]_i &= \frac{\exp([\tilde{\mathbf{W}}_{\text{N}}^g]_i)}{\exp([\tilde{\mathbf{W}}_{\text{N}}^g]_i) + \exp([\tilde{\mathbf{W}}_{\text{R}}^g]_i)}, \\ [\mathbf{W}_{\text{R}}^g]_i &= \frac{\exp([\tilde{\mathbf{W}}_{\text{R}}^g]_i)}{\exp([\tilde{\mathbf{W}}_{\text{N}}^g]_i) + \exp([\tilde{\mathbf{W}}_{\text{R}}^g]_i)}. \end{aligned} \quad (4)$$

where $[\cdot]_i$ denotes the selection of the i -th channel. Finally, we modulate the NIR features \mathbf{F}_{N} and the RGB ones \mathbf{F}_{R} with \mathbf{W}_{N}^g and \mathbf{W}_{R}^g , respectively, *i.e.*,

$$\mathbf{F}_{\text{N}}^g = \mathbf{W}_{\text{N}}^g \odot \mathbf{F}_{\text{N}}, \quad \mathbf{F}_{\text{R}}^g = \mathbf{W}_{\text{R}}^g \odot \mathbf{F}_{\text{R}}, \quad (5)$$

where $\mathbf{F}_{\text{N}}^g \in \mathbb{R}^{C \times H \times W}$ and $\mathbf{F}_{\text{R}}^g \in \mathbb{R}^{C \times H \times W}$ are the globally modulated NIR features and the RGB ones, respectively.

Local Modulation Module. The Local Modulation Module (LMM) should focus on the structure inconsistency between NIR images and RGB ones. We suggest increasing the receptive field to perceive more structure information from a range of neighboring pixels. In detail, LMM takes the globally modulated NIR features \mathbf{F}_{N}^g and the RGB ones \mathbf{F}_{R}^g as inputs to estimate the local NIR weights \mathbf{W}_{N}^l and the RGB ones \mathbf{W}_{R}^l , as shown in Fig. 4 (a). Without complex network design,

LMM is built upon GMM by replacing the 1×1 convolutional layer in 1×1 block to a large kernel depth-wise convolutional layer (DWConv) [43] for capturing more local information, as shown in Fig. 4 (c). Finally, \mathbf{W}_{N}^l and \mathbf{W}_{R}^l are employed to get the fused NIR and RGB feature \mathbf{F}_{NR} as,

$$\mathbf{F}_{\text{NR}} = \mathbf{W}_{\text{N}}^l \odot \mathbf{F}_{\text{N}}^g + \mathbf{W}_{\text{R}}^l \odot \mathbf{F}_{\text{R}}^g. \quad (6)$$

\mathbf{F}_{NR} is then passed to the decoder to output the final denoising result.

Discussion. As a problem-orientated design module, SFM can make better use of the supplementary information in NIR images, resulting in significantly improved performance on low-light RGB image denoising compared to the naive way (see Fig. 3 (b)). In addition, to take full advantage of advanced denoising network architectures [7], [8], [10], [24], we hope SFM can be easily and efficiently integrated into varying denoising backbones. Therefore, we intentionally avoid adopting computationally complex operations, and design it as simply and efficiently as possible. The compact and lightweight architecture makes it only add few parameters and computation costs. The related experiment results are presented in Sec. V.

C. Loss Function

We deploy SFM in each scale in multi-scale denoising architecture. To make SFM play a better role in every scale, we

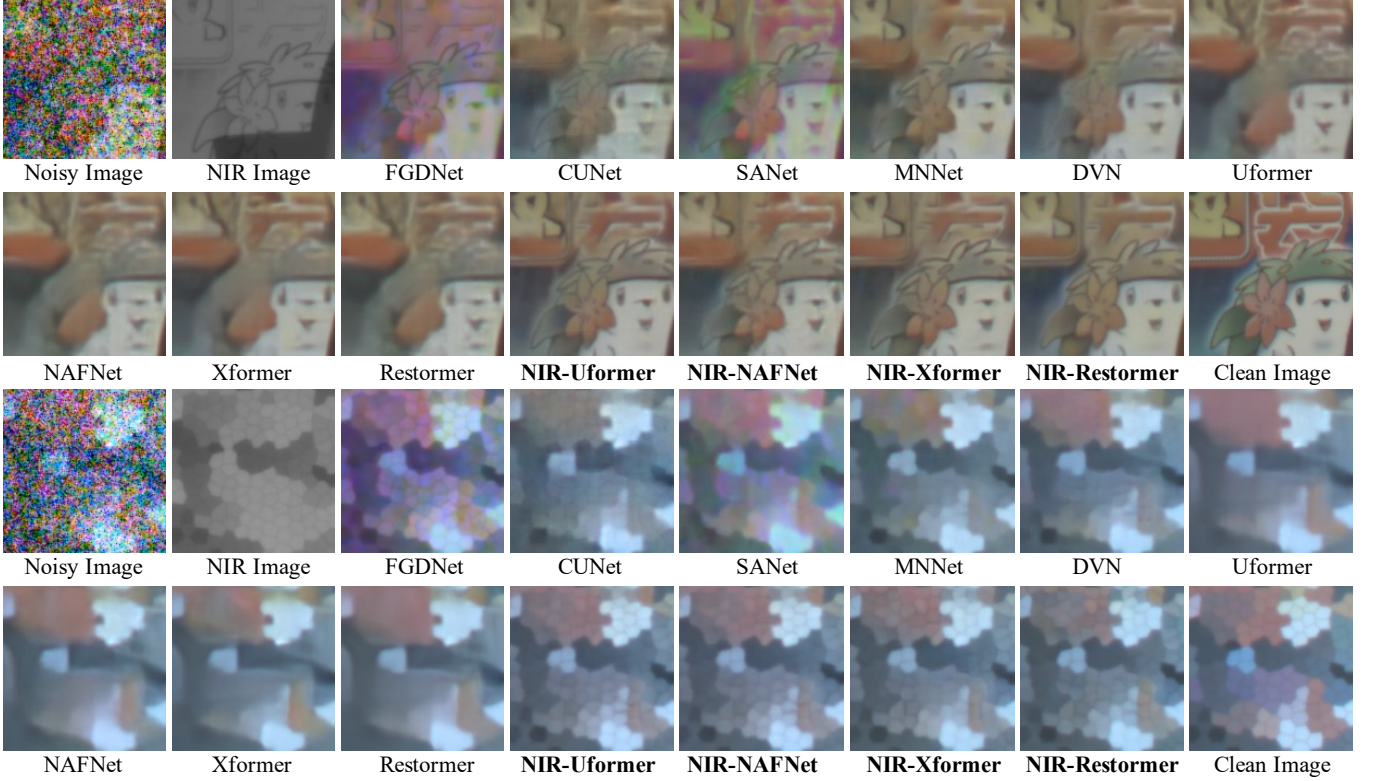


Fig. 5. Qualitative comparison on synthetic DVD dataset. **Bold** marks our methods.

TABLE II
QUANTITATIVE COMPARISON ON SYNTHETIC DVD DATASET. **BOLD** MARKS BEST RESULTS.

| Methods | $\sigma = 4$ | | $\sigma = 8$ | | #FLOPs (G) | Time (ms) |
|-----------------------------|--|--|--|--|------------|-----------|
| | PSNR \uparrow / SSIM \uparrow / LPIPS \downarrow | PSNR \uparrow / SSIM \uparrow / LPIPS \downarrow | PSNR \uparrow / SSIM \uparrow / LPIPS \downarrow | PSNR \uparrow / SSIM \uparrow / LPIPS \downarrow | | |
| Single-Image Denosing | Uformer (CVPR'22) | 29.58 / 0.8967 / 0.271 | 27.36 / 0.8632 / 0.352 | 19.16 | 1748 | |
| | Restormer (CVPR'22) | 29.67 / 0.9038 / 0.262 | 27.41 / 0.8741 / 0.343 | 70.59 | 2048 | |
| | NAFNet (ECCV'22) | 29.49 / 0.8959 / 0.263 | 27.29 / 0.8638 / 0.336 | 8.10 | 312 | |
| | Xformer (ICLR'24) | 27.32 / 0.8690 / 0.347 | 27.32 / 0.8690 / 0.347 | 73.31 | 5257 | |
| NIR-Assisted Image Denosing | FGDNet (TMM'22) | 23.91 / 0.8371 / 0.439 | 22.02 / 0.7374 / 0.436 | 38.67 | 479 | |
| | SANet (CVPR'23) | 27.68 / 0.8648 / 0.343 | 25.28 / 0.8304 / 0.413 | 161.06 | 2763 | |
| | CUNet(TPAMI'20) | 28.01 / 0.8558 / 0.332 | 26.07 / 0.8182 / 0.412 | 14.48 | 542 | |
| | MNNet (IF'22) | 28.48 / 0.8994 / 0.274 | 26.33 / 0.8697 / 0.353 | 23.68 | 1360 | |
| | DVN (AAAI'22) | 29.69 / 0.9062 / 0.236 | 27.43 / 0.8799 / 0.292 | 104.05 | 761 | |
| | NIR-Uformer (Ours) | 30.10 / 0.9188 / 0.192 | 28.03 / 0.9008 / 0.238 | 24.85 | 2500 | |
| | NIR-Restormer (Ours) | 30.22 / 0.9209 / 0.193 | 28.11 / 0.8701 / 0.260 | 89.17 | 2747 | |
| | NIR-NAFNet (Ours) | 30.08 / 0.9005 / 0.208 | 27.86 / 0.8664 / 0.273 | 13.17 | 462 | |
| | NIR-Xformer (Ours) | 30.29 / 0.9152 / 0.192 | 28.09 / 0.8947 / 0.230 | 95.63 | 7884 | |

adopt a multi-scale loss function to update network parameters, rather than a naive ℓ_1 or ℓ_2 loss. It can be written as,

$$\mathcal{L} = \sum_{s=1}^{S-1} \|\hat{\mathbf{I}}_s - \mathbf{I}_{\downarrow 2^{s-1}}\|_2. \quad (7)$$

Therein, S represents the number of network's scales. $\mathbf{I}_{\downarrow 2^{s-1}}$ denotes the target image after $\times 2^{s-1}$ down-sampling the ground truth. The output $\hat{\mathbf{I}}_s$ at scale s is generated from a 3×3 convolutional layer employed after the corresponding decoder, where $\hat{\mathbf{I}}_1$ represents the final result with full resolution.

V. EXPERIMENTS

A. Experimental Settings

Datasets. Experiments are conducted on the synthetic and our Real-NAID datasets. The details of the Real-NAID dataset can be seen in Sec. III. In addition, We use the DVD [19] dataset to generate synthetic noisy images. It comprises 307 pairs of clean RGB images (and corresponding RAW images) and NIR images. 267 pairs are used for training and 40 pairs are for testing. The way to simulate noisy data follows DVD [19]. We first scale the mean value of the clean RAW

TABLE III
QUANTITATIVE COMPARISON ON OUR REAL-NAID DATASET. **BOLD** MARKS BEST RESULTS.

| Methods | Low-Level Noise | | | Middle-Level Noise | | | High-Level Noise | | | |
|-----------------------|------------------------|-------------------------------|-------------------------------|-------------------------------|------------------------|-------------------------------|-------------------------------|------------------------|------------------------|-------------------------------|
| | PSNR↑ / SSIM↑ / LPIPS↓ | PSNR↑ / SSIM↑ / LPIPS↓ | PSNR↑ / SSIM↑ / LPIPS↓ | PSNR↑ / SSIM↑ / LPIPS↓ | PSNR↑ / SSIM↑ / LPIPS↓ | PSNR↑ / SSIM↑ / LPIPS↓ | PSNR↑ / SSIM↑ / LPIPS↓ | PSNR↑ / SSIM↑ / LPIPS↓ | PSNR↑ / SSIM↑ / LPIPS↓ | |
| Single-Image Denosing | Uformer (CVPR'22) | 25.56 / 0.7736 / 0.304 | 24.52 / 0.7418 / 0.347 | 23.31 / 0.7091 / 0.389 | 25.89 / 0.7842 / 0.294 | 24.98 / 0.7572 / 0.333 | 23.82 / 0.7297 / 0.387 | 25.71 / 0.7780 / 0.294 | 24.76 / 0.7482 / 0.335 | 23.71 / 0.7186 / 0.378 |
| | Xformer (ICLR'24) | 25.91 / 0.7804 / 0.292 | 24.81 / 0.7496 / 0.338 | 23.73 / 0.7201 / 0.382 | FGDNet (TMM'22) | 24.25 / 0.7676 / 0.368 | 22.89 / 0.7367 / 0.430 | 21.86 / 0.7080 / 0.509 | CUNet (TPAMI'20) | 24.05 / 0.7314 / 0.313 |
| | NAFNet (ECCV'22) | 25.71 / 0.7780 / 0.294 | 24.76 / 0.7482 / 0.335 | 23.69 / 0.7186 / 0.378 | SANet (CVPR'23) | 24.93 / 0.7679 / 0.359 | 23.74 / 0.7335 / 0.416 | 22.69 / 0.7028 / 0.476 | MNNet (IF'22) | 25.68 / 0.7797 / 0.313 |
| | DVN (AAAI'22) | 25.96 / 0.7853 / 0.298 | 24.93 / 0.7578 / 0.332 | 23.95 / 0.7360 / 0.382 | NIR-Uformer (Ours) | 25.91 / 0.7919 / 0.276 | 25.14 / 0.7714 / 0.299 | 24.28 / 0.7534 / 0.321 | NIR-Restormer (Ours) | 26.22 / 0.7963 / 0.265 |
| Image Denosing | NIR-NAFNet (Ours) | 26.06 / 0.7905 / 0.274 | 25.26 / 0.7676 / 0.303 | 24.48 / 0.7503 / 0.321 | NIR-Xformer (Ours) | 26.19 / 0.7959 / 0.264 | 25.38 / 0.7729 / 0.293 | 24.66 / 0.7595 / 0.319 | NIR-NAFNet (Ours) | 25.51 / 0.7767 / 0.293 |
| | NIR-Restormer (Ours) | 26.22 / 0.7963 / 0.265 | 25.51 / 0.7767 / 0.293 | 24.76 / 0.7626 / 0.315 | NIR-Xformer (Ours) | 26.19 / 0.7959 / 0.264 | 25.38 / 0.7729 / 0.293 | 24.66 / 0.7595 / 0.319 | NIR-NAFNet (Ours) | 25.51 / 0.7767 / 0.293 |

images, getting synthetic low-light clean RAW images. Then we add Gaussian noise with the variance σ and Poisson noise with a noise level σ to the generated low-light images. Finally, the synthetic low-light noisy RAW images are converted to RGB ones for training models. We conduct experiments with $\sigma = 4$ and $\sigma = 8$ (the larger σ , the heavier noise).

Implementation Details. We build our NIR-assisted denoising models by incorporating the proposed SFM into a CNN-based advanced denoising network (*i.e.*, NAFNet [24]) and three Transformer-based ones (*i.e.*, Uformer [8], Restormer [7] and Xformer [10]), which are dubbed **NIR-NAFNet**, **NIR-Uformer**, **NIR-Restormer**, and **NIR-Xformer**, respectively. All models are trained by the Adam [44] optimizer with $\beta_1 = 0.9$ and $\beta_2 = 0.999$ for 120k iterations. The batch size is set to 32 and the patch size is set to 128×128 . For synthetic image denoising, the cosine annealing strategy [45] is employed to steadily decrease the learning rate from 2×10^{-4} to 1×10^{-6} . For real-world image denoising, the initial learning rate is set to 3×10^{-4} and halved every 20k iterations. All experiments are conducted with PyTorch [46] on an Nvidia GeForce RTX A6000 GPU.

B. Comparison with State-of-the-Art Methods

Experiments are conducted by comparing our NIR-NAFNet, NIR-Uformer, NIR-Restormer, and NIR-Xformer with 9 models, including 4 single image denoising methods (*i.e.* NAFNet [24], Uformer [8], Restormer [7], and Xformer [10]) and 5 NIR-assisted image denoising methods (*i.e.* FGDNet [47], SANet [23], CUNet [36], MNNet [48], and DVN [19]). To evaluate the performance quantitatively, we calculate three metrics on the RGB channels, *i.e.*, Peak Signal to Noise Ratio (PSNR), Structural Similarity (SSIM) [49] and Learned Perceptual Image Patch Similarity (LPIPS) [50]. We also evaluate the inference cost of different models. The #FLOPs when processing a 128×128 patch and the inference time when feeding a 1792×1008 image are reported.

Results on Synthetic DVD dataset. The quantitative results on the synthetic DVD dataset are shown in Table II. The best results are shown in bold. It can be observed that our

method significantly improves performance against single-image denoising methods, thereby demonstrating the effectiveness of NIR images. In comparison with existing NIR-assisted denoising ones, our methods also outperform by a large margin, as the proposed SFM overcomes the discrepancy issues between the NIR-RGB images while coupling with the advanced denoising backbone successfully. In particular, our NIR-NAFNet makes a better trade-off between performance and efficiency than other methods. Besides, The qualitative results in Fig. 5 show that our methods restore more realistic textures and fewer artifacts than others.

Results on Real-NAID Dataset. Real-world data has much more complex degradation than synthetic ones. The quantitative results in Table III show that our methods still keep high performance in the real world. Taking NIR-Restormer as an example, our proposed NIR-Restormer achieves 0.33dB, 0.54dB, and 0.94dB PSNR gains than Restormer [7] in dealing with low-level, middle-level and high-level noise, respectively. The higher the level of noise, the greater the improvement achieved by our method, which further indicates the advantage of the utilization of NIR information for low-light noise removal. The qualitative results in Fig. 6 demonstrate that our models still recover fine-scale details in the real world, while other NIR-assisted denoising methods may produce artifacts.

VI. ABLATION STUDY

We conduct ablation studies on our Real-NAID dataset using NIR-NAFNet. Unless otherwise stated, ablation experiments are evaluated at three noise levels, and the metrics are reported by averaging them on three noise levels. The experiments include comparisons with NAID baselines, comparisons with more fusion manners, effect of SFM, and effect of multi-scale loss.

A. Comparisons with NAID Baselines

To demonstrate the effectiveness of our SFM, we compare our methods with NAID baselines using varying backbones. Specifically, we simply sum the NIR and RGB features as our

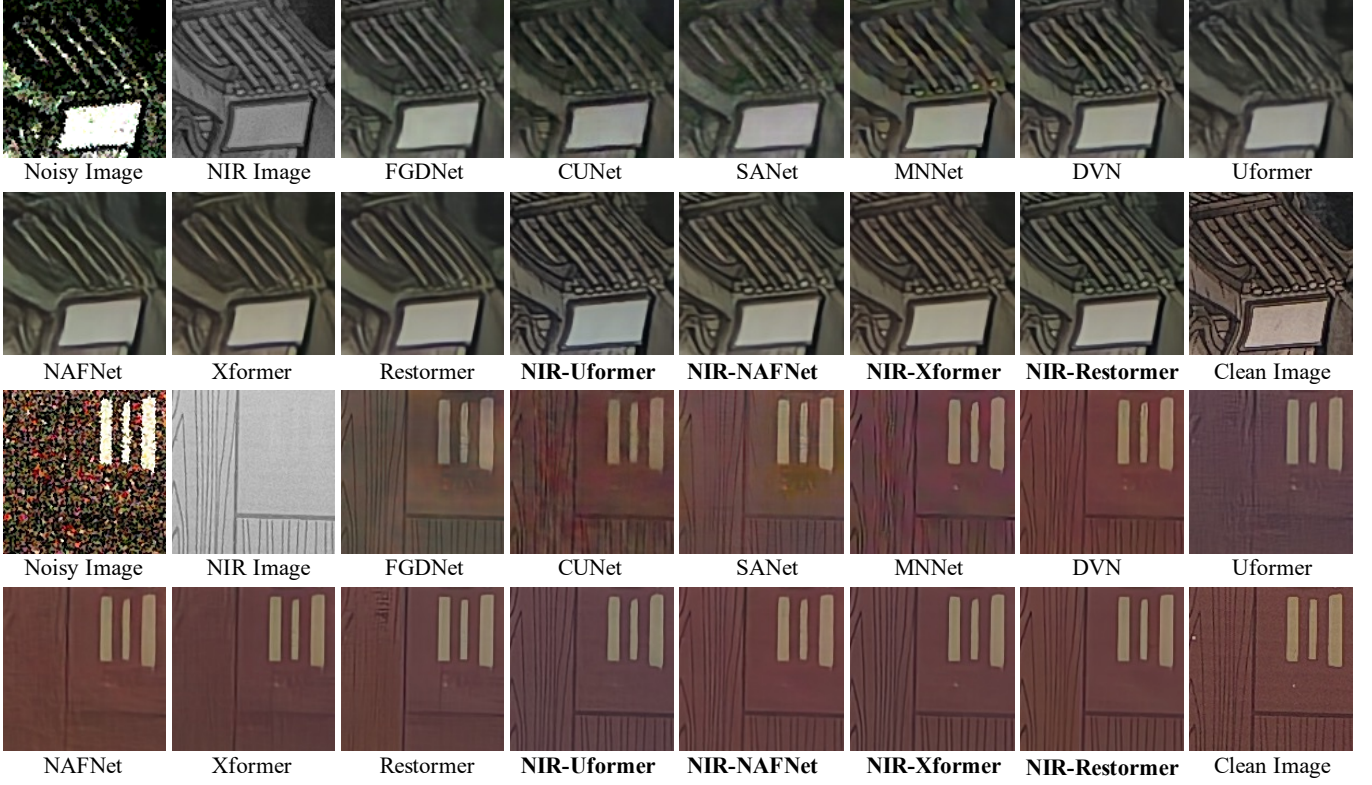


Fig. 6. Qualitative comparison on our Real-NAID dataset. **Bold** marks our methods.

TABLE IV
COMPARISONS OF OUR PROPOSED METHOD WITH THE NAID BASELINES (SEE FIG. 3 (B)) ON DIFFERENT BACKBONES ON OUR REAL-NVID DATASET.

| Methods | Low-Level Noise | | | Middle-Level Noise | | | High-Level Noise | | |
|------------------------------------|----------------------|------------------------|------------------------|------------------------|----------------------|----------------------|----------------------|----------------------|----------------------|
| | PSNR↑/ SSIM↑/ LPIPS↓ | PSNR↑/ SSIM↑/ LPIPS↓ | PSNR↑/ SSIM↑/ LPIPS↓ | PSNR↑/ SSIM↑/ LPIPS↓ | PSNR↑/ SSIM↑/ LPIPS↓ | PSNR↑/ SSIM↑/ LPIPS↓ | PSNR↑/ SSIM↑/ LPIPS↓ | PSNR↑/ SSIM↑/ LPIPS↓ | PSNR↑/ SSIM↑/ LPIPS↓ |
| Spatial-Wised Transformer-Based | Uformer-Baseline | 25.80 / 0.7904 / 0.269 | 25.03 / 0.7687 / 0.294 | 24.02 / 0.7488 / 0.320 | | | | | |
| | NIR-Uformer | 25.91 / 0.7917 / 0.276 | 25.14 / 0.7714 / 0.299 | 24.28 / 0.7534 / 0.321 | | | | | |
| Channel-Wised Transformer-Based | Restormer-Baseline | 26.12 / 0.7948 / 0.265 | 25.38 / 0.7733 / 0.293 | 24.61 / 0.7587 / 0.316 | | | | | |
| | NIR-Restormer | 26.22 / 0.7963 / 0.265 | 25.51 / 0.7767 / 0.293 | 24.76 / 0.7626 / 0.315 | | | | | |
| Mixed Transformer-Based | Xformer-Baseline | 26.10 / 0.7927 / 0.264 | 25.23 / 0.7694 / 0.291 | 24.41 / 0.7553 / 0.314 | | | | | |
| | NIR-Xformer | 26.19 / 0.7959 / 0.264 | 25.38 / 0.7729 / 0.293 | 24.66 / 0.7595 / 0.319 | | | | | |
| CNN-Based | NAFNet-Baseline | 25.92 / 0.7883 / 0.277 | 25.00 / 0.7628 / 0.304 | 24.16 / 0.7429 / 0.329 | | | | | |
| | NIR-NAFNet | 26.06 / 0.7905 / 0.274 | 25.26 / 0.7676 / 0.303 | 24.48 / 0.7503 / 0.321 | | | | | |

baseline, as shown in Fig. 3 (b). We utilize three Transformer-based denoising networks (*i.e.*, Uformer [8], Restormer [7], Xformer [10]) and a CNN-based one (*i.e.*, NAFNet [24]) to conduct experiments, named ‘Uformer-Baseline’, ‘Restormer-Baseline’, ‘Xformer-Baseline’, and ‘NAFNet-Baseline’, respectively. From Table IV, it is observed that the performance of NAID baselines can be further improved by integrating our proposed SFM, and the improvement is more significant when the noise level is higher. This is because that simple summation in NAID baselines ignores color and structure discrepancies between NIR-RGB images while the proposed SFM alleviates these issues.

B. Comparisons with More Fusion Manners

We compare our selective fusion manner with other fusion methods, including feature summation, channel attention [51],

TABLE V
COMPARISONS WITH MORE FUSION MANNERS.

| Input Images | Fusion Methods | PSNR↑/ SSIM↑/ LPIPS↓ | Time (ms) |
|--------------|----------------|------------------------|-----------|
| RGB | None | 24.72 / 0.7486 / 0.336 | 312 |
| RGB and NIR | Sum | 25.03 / 0.7647 / 0.304 | 461 |
| RGB and NIR | Channel Att. | 25.12 / 0.7664 / 0.309 | 461 |
| RGB and NIR | Cross Att. | 25.18 / 0.7692 / 0.304 | 1712 |
| RGB and NIR | Ours | 25.26 / 0.7695 / 0.299 | 462 |

and cross attention [52] to demonstrate our method’s superiority. The results on Real-NAID dataset are shown in Table V. It can be observed the usage of NIR images and other prevailing fusion methods can improve performance to some degree. However, these methods do not achieve competitive performance compared with our SFM while sometimes introducing

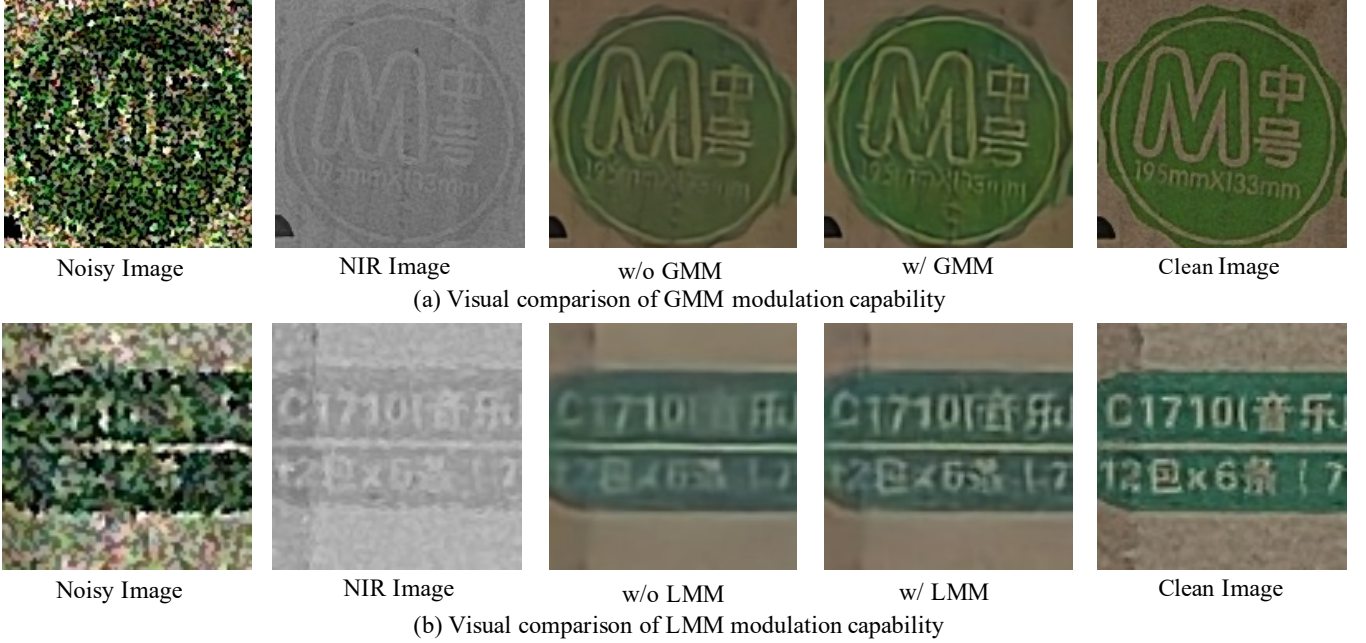


Fig. 7. (a) Visual comparison of GMM modulation capability. GMM tends to modulate global color. (b) Visual comparison of LMM modulation capability. LMM tends to modulate local structure.

TABLE VI
QUANTITATIVE COMPARISON WITH DIFFERENT MODULATION MODULES IN SFM.

| GMM | LMM | PSNR↑ / SSIM↑ / LPIPS↓ |
|-----|-----|------------------------|
| ✗ | ✗ | 25.03 / 0.7647 / 0.304 |
| ✓ | ✗ | 25.16 / 0.7675 / 0.302 |
| ✗ | ✓ | 25.16 / 0.7653 / 0.302 |
| ✓ | ✓ | 25.26 / 0.7695 / 0.299 |

TABLE VIII
QUANTITATIVE COMPARISON OF DIFFERENT ARRANGEMENTS OF GMM AND LMM.

| Arrangement | PSNR↑ / SSIM↑ / LPIPS↓ |
|-------------|------------------------|
| GMM + GMM | 25.17 / 0.7652 / 0.302 |
| LMM + LMM | 25.18 / 0.7650 / 0.301 |
| LMM + GMM | 25.19 / 0.7669 / 0.301 |
| GMM + LMM | 25.26 / 0.7695 / 0.299 |

TABLE VII
QUANTITATIVE COMPARISON OF DIFFERENT KERNEL SIZES OF DWCONV IN LMM.

| Kernel Size | PSNR↑ / SSIM↑ / LPIPS↓ |
|-------------|------------------------|
| 3 × 3 | 25.22 / 0.7685 / 0.298 |
| 5 × 5 | 25.26 / 0.7695 / 0.299 |
| 7 × 7 | 25.28 / 0.7717 / 0.301 |

higher computation costs. It illustrates the superiority of the proposed method.

C. Effect of SFM

To illustrate the effect of SFM, we conduct a more detailed investigation and exploration on GMM and LMM.

Effect of GMM. As shown in Table VI, the incorporation of GMM yields 0.13dB PSNR improvement on its own and yields 0.1dB PSNR improvement on the basis of LMM, which can be attributed to its effective handling of the inconsistency between NIR-RGB images in color. Additionally, we provide a visual comparison to demonstrate the impact of GMM on visual results. As shown in Fig. 7 (a), the incorporation of our GMM helps better color recovery.

Effect of LMM. As shown in Table VI, there is a 0.1dB drop on PSNR when removing LMM from SFM. We provide

a qualitative result to demonstrate its impact on visual results. As shown in Fig. 7 (b), the incorporation of our LMM in SFM helps fine-scale texture recovery. Moreover, we explore the appropriate receptive field size in LMM by employing varying kernel sizes of DWConv as shown in Table VII. Generally, a larger kernel size leads to greater performance improvement, which shows that a large reception field helps the local modulation of features. But it is improved marginally when the kernel size is larger than 5 × 5. For the sake of simplicity and efficiency, we set the kernel size of DWConv to 5 × 5 as default.

Effect of GMM and LMM Arrangement. Here, we conduct experiments with different arrangements of GMM and LMM. The results are shown in Table VIII. ‘GMM + GMM’ and ‘LMM + LMM’ mean we modulate features with 2 GMMs and 2 LMMs respectively. They result in limited performance gain. It shows that our performance improvement is not due to a simple increase in parameter numbers. ‘LMM + GMM’ means we modulate features first locally and then globally. It also leads to limited improvement. It may be because the significant difference in global content leads to inaccurate local feature modulation. Therefore, we deploy a GMM to handle color discrepancy first followed by an LMM dealing with structure discrepancy, dubbed ‘GMM + LMM’, achieving

TABLE IX
QUANTITATIVE COMPARISON OF DIFFERENT NUMBERS OF SFM.

| #SFM | PSNR \uparrow / SSIM \uparrow / LPIPS \downarrow |
|------|--|
| 1 | 25.26 / 0.7695 / 0.299 |
| 3 | 25.28 / 0.7699 / 0.299 |
| 5 | 25.29 / 0.7669 / 0.301 |

TABLE X
COMPARISONS OF DIFFERENT LOSS FUNCTIONS.

| Input Images | Loss Function | PSNR \uparrow / SSIM \uparrow / LPIPS \downarrow |
|--------------|----------------|--|
| RGB | Naive ℓ_2 | 24.72 / 0.7476 / 0.343 |
| RGB | Multi-Scale | 24.73 / 0.7483 / 0.336 |
| RGB and NIR | Naive ℓ_2 | 25.20 / 0.7691 / 0.299 |
| RGB and NIR | Multi-Scale | 25.26 / 0.7695 / 0.299 |

better results.

Effect of Number of SFM. Here we investigate the effect of incorporating multiple SFMs at each scale of NIR-NAFNet. The results are shown in Table IX. It can be observed that the performance generally increases marginally as the number of SFMs grows. Also for the sake of simplicity and efficiency, we only set the number of SFM to 1 at each scale.

Efficiency of GMM and LMM. Both GMM and LMM are lightweight modules that do not increase the number of parameters and inference time too much. The number of parameters of GMM and LMM only account for 1.5% and 1.1% of those of NIR-NAFNet, respectively. Applying an SFM on NIR-NAFNet only results in a time increase of 1 ms.

D. Effect of Multi-Scale Loss

The multi-scale loss calculates the difference between output and supervision at different scales, and it can slightly improve performance with few increasing training costs. Taking NAFNet [24] as an example, we evaluate its effect by comparing it with naive ℓ_2 loss. Table X shows that it improves the performance of both single-image and NIR-assisted image denoising. And the improvement is more obvious for the latter. This shows that multi-scale loss can help SFM work better at each scale.

VII. CONCLUSION

Near-infrared (NIR) images can help restore fine-scale details while removing noise from noisy RGB images, especially in low-light environments. The content inconsistency between NIR-RGB images and the scarcity of real-world paired datasets limit its effective application in real scenarios. In this work, we propose a plug-and-play Selective Fusion Module (SFM) and a Real-world NIR-Assisted Image Denoising (Real-NAID) dataset to address these issues. Specifically, SFM sequentially performs global and local modulations on NIR-RGB features before their information fusion. The Real-NAID dataset is collected with various noise levels under diverse scenes. Experiments on both synthetic and our real-world datasets show the proposed method achieves better results than state-of-the-art ones.

ACKNOWLEDGMENTS

This work was supported by the National Natural Science Foundation of China (NSFC) under Grants No. U19A2073.

REFERENCES

- [1] K. He, X. Zhang, S. Ren, and J. Sun, “Deep residual learning for image recognition,” in *CVPR*, 2016.
- [2] J. Liang, J. Cao, G. Sun, K. Zhang, L. Van Gool, and R. Timofte, “Swinir: Image restoration using swin transformer,” in *ICCV*, 2021.
- [3] A. Vaswani, N. Shazeer, N. Parmar, J. Uszkoreit, L. Jones, A. N. Gomez, Ł. Kaiser, and I. Polosukhin, “Attention is all you need,” *NeurIPS*, 2017.
- [4] K. Zhang, W. Zuo, Y. Chen, D. Meng, and L. Zhang, “Beyond a gaussian denoiser: Residual learning of deep cnn for image denoising,” *IEEE transactions on image processing*, vol. 26, no. 7, pp. 3142–3155, 2017.
- [5] K. Zhang, W. Zuo, and L. Zhang, “Ffdnet: Toward a fast and flexible solution for cnn-based image denoising,” *IEEE Transactions on Image Processing*, vol. 27, no. 9, pp. 4608–4622, 2018.
- [6] A. Abdelhamed, M. Afifi, R. Timofte, and M. S. Brown, “Ntire 2020 challenge on real image denoising: Dataset, methods and results,” in *CVPR Workshops*, 2020, pp. 496–497.
- [7] S. W. Zamir, A. Arora, S. Khan, M. Hayat, F. S. Khan, and M.-H. Yang, “Restormer: Efficient transformer for high-resolution image restoration,” in *Proceedings of the IEEE/CVF conference on computer vision and pattern recognition*, 2022, pp. 5728–5739.
- [8] Z. Wang, X. Cun, J. Bao, W. Zhou, J. Liu, and H. Li, “Uformer: A general u-shaped transformer for image restoration,” in *Proceedings of the IEEE/CVF conference on computer vision and pattern recognition*, 2022, pp. 17683–17693.
- [9] J. Li, Z. Zhang, X. Liu, C. Feng, X. Wang, L. Lei, and W. Zuo, “Spatially adaptive self-supervised learning for real-world image denoising,” in *CVPR*, 2023.
- [10] J. Zhang, Y. Zhang, J. Gu, J. Dong, L. Kong, and X. Yang, “Xformer: Hybrid x-shaped transformer for image denoising,” *arXiv preprint arXiv:2303.06440*, 2023.
- [11] B. Mildenhall, J. T. Barron, J. Chen, D. Sharlet, R. Ng, and R. Carroll, “Burst denoising with kernel prediction networks,” in *Proceedings of the IEEE conference on computer vision and pattern recognition*, 2018, pp. 2502–2510.
- [12] C. Godard, K. Matzen, and M. Uyttendaele, “Deep burst denoising,” in *Proceedings of the European conference on computer vision (ECCV)*, 2018, pp. 538–554.
- [13] N. Pearl, T. Treibitz, and S. Korman, “Nan: Noise-aware nerfs for burst-denoising,” in *Proceedings of the IEEE/CVF Conference on Computer Vision and Pattern Recognition*, 2022, pp. 12672–12681.
- [14] R. Wu, Z. Zhang, S. Zhang, H. Zhang, and W. Zuo, “Rbsr: Efficient and flexible recurrent network for burst super-resolution,” in *Chinese Conference on Pattern Recognition and Computer Vision (PRCV)*. Springer, 2023, pp. 65–78.
- [15] Z. Zhang, R. Xu, M. Liu, Z. Yan, and W. Zuo, “Self-supervised image restoration with blurry and noisy pairs,” *Advances in Neural Information Processing Systems*, vol. 35, pp. 29179–29191, 2022.
- [16] Z. Zhang, S. Zhang, R. Wu, Z. Yan, and W. Zuo, “Exposure bracketing is all you need for unifying image restoration and enhancement tasks,” *arXiv preprint arXiv:2401.00766*, 2024.
- [17] F. Lv, Y. Zheng, Y. Li, and F. Lu, “An integrated enhancement solution for 24-hour color imaging,” in *Proceedings of the AAAI conference on artificial intelligence*, 2020, pp. 11725–11732.
- [18] G. Wu, Y. Zheng, Z. Guo, Z. Cai, X. Shi, X. Ding, Y. Huang, Y. Guo, and R. Shibasaki, “Learn to recover visible color for video surveillance in a day,” in *Computer Vision–ECCV 2020: 16th European Conference, Glasgow, UK, August 23–28, 2020, Proceedings, Part I 16*. Springer, 2020, pp. 495–511.
- [19] S. Jin, B. Yu, M. Jing, Y. Zhou, J. Liang, and R. Ji, “Darkvisionnet: Low-light imaging via rgb-nir fusion with deep inconsistency prior,” in *Proceedings of the AAAI Conference on Artificial Intelligence*, 2022, pp. 1104–1112.
- [20] R. Wan, B. Shi, W. Yang, B. Wen, L.-Y. Duan, and A. C. Kot, “Purifying low-light images via near-infrared enlightened image,” *IEEE Transactions on Multimedia*, 2022.
- [21] C. Fredembach and S. Süstrunk, “Colouring the near infrared,” in *Proceedings of the IS&T/SID 16th Color Imaging Conference*, 2008, pp. 176–182.
- [22] J. Xiong, J. Wang, W. Heidrich, and S. Nayar, “Seeing in extra darkness using a deep-red flash,” in *CVPR*, 2021, pp. 10000–10009.

[23] Z. Sheng, Z. Yu, X. Liu, S.-Y. Cao, Y. Liu, H.-L. Shen, and H. Zhang, “Structure aggregation for cross-spectral stereo image guided denoising,” in *Proceedings of the IEEE/CVF Conference on Computer Vision and Pattern Recognition*, 2023, pp. 13 997–14 006.

[24] L. Chen, X. Chu, X. Zhang, and J. Sun, “Simple baselines for image restoration,” in *European Conference on Computer Vision*. Springer, 2022, pp. 17–33.

[25] O. Ronneberger, P. Fischer, and T. Brox, “U-net: Convolutional networks for biomedical image segmentation,” in *MICCAI*. Springer, 2015.

[26] H. Chen, Y. Wang, T. Guo, C. Xu, Y. Deng, Z. Liu, S. Ma, C. Xu, C. Xu, and W. Gao, “Pre-trained image processing transformer,” in *CVPR*, 2021.

[27] A. Buades, B. Coll, and J.-M. Morel, “A non-local algorithm for image denoising,” in *2005 IEEE computer society conference on computer vision and pattern recognition (CVPR’05)*, vol. 2. Ieee, 2005, pp. 60–65.

[28] K. Dabov, A. Foi, V. Katkovnik, and K. Egiazarian, “Image denoising by sparse 3-d transform-domain collaborative filtering,” *IEEE Transactions on image processing*, vol. 16, no. 8, pp. 2080–2095, 2007.

[29] S. Gu, L. Zhang, W. Zuo, and X. Feng, “Weighted nuclear norm minimization with application to image denoising,” in *Proceedings of the IEEE conference on computer vision and pattern recognition*, 2014, pp. 2862–2869.

[30] S. W. Zamir, A. Arora, S. Khan, M. Hayat, F. S. Khan, M.-H. Yang, and L. Shao, “Multi-stage progressive image restoration,” in *Proceedings of the IEEE/CVF conference on computer vision and pattern recognition*, 2021, pp. 14 821–14 831.

[31] D. Krishnan and R. Fergus, “Dark flash photography,” *ACM Trans. Graph.*, vol. 28, no. 3, jul 2009. [Online]. Available: <https://doi.org/10.1145/1531326.1531402>

[32] X. Wang, F. Dai, Y. Ma, J. Guo, Q. Zhao, and Y. Zhang, “Near-infrared image guided neural networks for color image denoising,” in *ICASSP 2019-2019 IEEE International Conference on Acoustics, Speech and Signal Processing (ICASSP)*. IEEE, 2019, pp. 3807–3811.

[33] Y. Yang, J. Liu, S. Huang, W. Wan, W. Wen, and J. Guan, “Infrared and visible image fusion via texture conditional generative adversarial network,” *IEEE Transactions on Circuits and Systems for Video Technology*, vol. 31, no. 12, pp. 4771–4783, 2021.

[34] Y. Cheng, R. Yang, Z. Zhang, J. Suo, and Q. Dai, “A mutually boosting dual sensor computational camera for high quality dark videography,” *Information Fusion*, vol. 93, pp. 429–440, 2023.

[35] Z. Zhao, H. Bai, J. Zhang, Y. Zhang, S. Xu, Z. Lin, R. Timofte, and L. Van Gool, “Cddfuse: Correlation-driven dual-branch feature decomposition for multi-modality image fusion,” in *Proceedings of the IEEE/CVF Conference on Computer Vision and Pattern Recognition*, 2023, pp. 5906–5916.

[36] X. Deng and P. L. Dragotti, “Deep convolutional neural network for multi-modal image restoration and fusion,” *IEEE transactions on pattern analysis and machine intelligence*, vol. 43, no. 10, pp. 3333–3348, 2020.

[37] S. Xu, J. Zhang, J. Wang, K. Sun, C. Zhang, J. Liu, and J. Hu, “A model-driven network for guided image denoising,” *Information Fusion*, vol. 85, pp. 60–71, 2022.

[38] M. Brown and S. Süsstrunk, “Multi-spectral sift for scene category recognition,” in *CVPR 2011*. IEEE, 2011, pp. 177–184.

[39] T. Zhi, B. R. Pires, M. Hebert, and S. G. Narasimhan, “Deep material-aware cross-spectral stereo matching,” in *Proceedings of the IEEE conference on computer vision and pattern recognition*, 2018, pp. 1916–1925.

[40] J. Wang, T. Xue, J. T. Barron, and J. Chen, “Stereoscopic dark flash for low-light photography,” in *2019 IEEE International Conference on Computational Photography (ICCP)*. IEEE, 2019, pp. 1–10.

[41] J. L. Ba, J. R. Kiros, and G. E. Hinton, “Layer normalization,” *arXiv preprint arXiv:1607.06450*, 2016.

[42] K. He, X. Zhang, S. Ren, and J. Sun, “Delving deep into rectifiers: Surpassing human-level performance on imagenet classification,” in *ICCV*, 2015, pp. 1026–1034.

[43] A. G. Howard, M. Zhu, B. Chen, D. Kalenichenko, W. Wang, T. Weyand, M. Andreetto, and H. Adam, “Mobilennets: Efficient convolutional neural networks for mobile vision applications,” *arXiv preprint arXiv:1704.04861*, 2017.

[44] D. P. Kingma and J. Ba, “Adam: A method for stochastic optimization,” *arXiv preprint arXiv:1412.6980*, 2014.

[45] I. Loshchilov and F. Hutter, “Decoupled weight decay regularization,” *arXiv preprint arXiv:1711.05101*, 2017.

[46] A. Paszke, S. Gross, F. Massa, A. Lerer, J. Bradbury, G. Chanan, T. Killeen, Z. Lin, N. Gimelshein, L. Antiga *et al.*, “Pytorch: An imperative style, high-performance deep learning library,” *Advances in neural information processing systems*, vol. 32, 2019.

[47] Z. Sheng, X. Liu, S.-Y. Cao, H.-L. Shen, and H. Zhang, “Frequency-domain deep guided image denoising,” *IEEE Transactions on Multimedia*, 2022.

[48] S. Xu, J. Zhang, J. Wang, K. Sun, C. Zhang, J. Liu, and J. Hu, “A model-driven network for guided image denoising,” *Information Fusion*, vol. 85, pp. 60–71, 2022.

[49] Z. Wang, A. C. Bovik, H. R. Sheikh, and E. P. Simoncelli, “Image quality assessment: from error visibility to structural similarity,” *IEEE transactions on image processing*, vol. 13, no. 4, pp. 600–612, 2004.

[50] R. Zhang, P. Isola, A. A. Efros, E. Shechtman, and O. Wang, “The unreasonable effectiveness of deep features as a perceptual metric,” in *CVPR*, 2018, pp. 586–595.

[51] Y. Zhang, K. Li, K. Li, L. Wang, B. Zhong, and Y. Fu, “Image super-resolution using very deep residual channel attention networks,” in *ECCV*, 2018, pp. 286–301.

[52] Z. Liu, Y. Lin, Y. Cao, H. Hu, Y. Wei, Z. Zhang, S. Lin, and B. Guo, “Swin transformer: Hierarchical vision transformer using shifted windows,” in *ICCV*, 2021, pp. 10 012–10 022.